ACS Sustainable Chemistry & Engineering

pubs.acs.org/journal/ascecg

Research Article

Efficient Recovery of Gold(I) from Thiosulfate Solutions through Photocatalytic Reduction with Mn(II)-Doped MoS_2

Weiquan Zhan, Yuan Yuan, Xin Yao, Bingqiao Yang, Feifei Jia,* Changsheng Lin, José Luis Arauz-Lara, and Shaoxian Song

Cite This: https://doi.org/10.1021/acssuschemeng.1c02160

Read Online

ACCESS | Metrics & More | Article Recommendations

ABSTRACT: Developing efficient materials for the extraction of gold(I) was pivotal for application of ammoniacal thiosulfate leaching technology. Mn-doped molybdenum disulfide (Mn-MoS_2) spheres were fabricated by a facile hydrothermal route for photocatalytic reduction of the gold(I) thiosulfate complex ($[Au(S_2O_3)_2]^{3-}$) in this work. The experimental results exhibited that $[Au(S_2O_3)_2]^{3-}$ was efficiently recycled in the form of gold nanoparticles by Mn-MoS_2. The reduction capacity (936.9 mg/g) and rate (2.74 mg/(g min) in 300 min) was 1.5 and 2.72 times higher than that of MoS_2, respectively. The inside photocatalytic reduction mechanism was studied by combining an experimental and first-principles approach. Outstanding reduction performance of $[Au(S_2O_3)_2]^{3-}$ was attributed to the enhanced transfer of photoinduced electrons after Mn doping. In addition, S atoms in the Mn-S bond could well interact with Au(I), which slightly promoted the adsorption of $[Au(S_2O_3)_2]^{3-}$ on Mn-MoS_2. The discovery provided a promising strategy for the efficient extraction of gold(I) from thiosulfate leaching solutions.

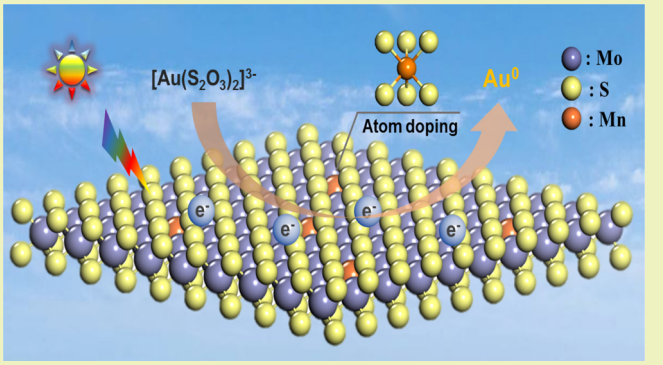

KEYWORDS: *photocatalytic reduction, gold(I) thiosulfate complex, Mn doping, molybdenum disulfide*

1. INTRODUCTION

Until now, cyanide leaching was widely applied for extracting gold,[1,2] which was harmful for the environment owing to the high toxicity of cyanide.[3] As the world advocated and promoted green development, it was urgent to develop an eco-friendly and efficient technique for leaching gold instead of cyanide leaching. Ammoniacal thiosulfate leaching technique recently received increasing attentions, as it exhibited many obvious advantages, such as nontoxicity, low cost, and eco-friendliness.[4] However, the existing three main problems (high reagent consumption; challenging recovery of $[Au(S_2O_3)_2]^{3-}$; and high concentration of ammonia used) had led to the difficulty in industrial application.[5] Among these problems, efficient recovery of $[Au(S_2O_3)_2]^{3-}$ was a major research topic.

A wide range of techniques including cementation,[6] metal displacement,[7] and ion-exchange[8] had been applied for recycling $[Au(S_2O_3)_2]^{3-}$ from leaching solutions, but high cost and inefficient recovery limited their actual applications. Although adsorption won the most attention with its simplicity, high efficiency, and low cost,[9] most adsorbents like activated carbon,[10] modified activated carbon,[11] and thiol- and amine-functionalized mesoporous silica[12] did not exhibit good recovery. Lately, a photocatalytic reduction method combining adsorption and reduction procedures has been proposed for simplifying the recovery steps and enhancing the recovery.[13−15]

MoS_2, having nontoxicity, low cost, abundance, and inherent band gaps, was an attractive material in the catalysis field.[16] Based on the hard soft acid base principle and electrochemistry basic principle (conduction band (CB) of MoS_2[17] was lower in energy than the reduction potential of $[Au(S_2O_3)_2]^{3-}$ to Au^0[18]), sulfur-rich MoS_2 exhibited good adsorption[19] and photocatalytic reduction ability[20] of $[Au(S_2O_3)_2]^{3-}$. The reduction of $[Au(S_2O_3)_2]^{3-}$ by MoS_2 mainly consisted of photoreduction and chemical reduction in which photo-reduction played a dominant role.[21] What is more, MoS_2 could be reused from liquid through construction of three-dimensional aerogels or combing with magnetic material such as Fe_3O_4.[22]

From the perspective of catalysis using MoS_2, the electronic conductivity of MoS_2 was unsatisfactory,[23−25] which might

Received: March 30, 2021
Revised: August 12, 2021

hinder further efficient recovery of $[Au(S_2O_3)_2]^{3-}$. Doping with heteroatoms in MoS_2 had always been considered one of the most promising strategy to tune the electronic structure and then improve the photocatalytic reduction ability.[26−28] Transition metal atoms such as Co, Ni, Mn, Se, etc. were employed to incorporate into MoS_2 for enhancing the electronic conductivity in both experimental and theoretical works.[28,29] Among the transition metal atom dopants, Mn atoms possessed these advantages: cheap sources and well matching the structure of MoS_2. To our knowledge, no attempt had been made to incorporate transition metal atoms into MoS_2 as a catalyst for extracting Au(I) from thiosulfate solutions.

Herein, a Mn dopant was adopted as a regulatory factor to optimize the electronic status and active sites of MoS_2 for achieving high reduction of $[Au(S_2O_3)_2]^{3-}$. Flowerlike Mn-MoS_2 spheres were obtained by a hydrothermal method. The morphology, chemical component, and microstructure of Mn-incorporated MoS_2 spheres were observed through X-ray diffraction (XRD), scanning electron microscopy (SEM), X-ray photoelectron spectroscopy (XPS), and transmission electron microscopy (TEM). The reduction behaviors and mechanism of $[Au(S_2O_3)_2]^{3-}$ on Mn-MoS_2 were well investigated through batch experiments, TEM, photocurrent tests, ultraviolet−visible (UV−vis) absorption, and density functional theory (DFT) calculations. The aim was to build a better understanding of the promoted recovery of $[Au(S_2O_3)_2]^{3-}$ in aqueous solutions by Mn-MoS_2, paving a new strategy toward the recycling of gold(I) from thiosulfate-leaching solutions.

2. EXPERIMENTAL SECTION

2.1. Material. The reagents used for preparing Mn-MoS_2 spheres including ammonium molybdate tetrahydrate ($(NH_4)_6Mo_7O_{24}\cdot 4H_2O$), thiourea ($CN_2H_4S$), sodium hydroxide (NaOH), and manganese chloride tetrahydrate ($MnCl_2\cdot 4H_2O$) were all purchased from Sinopharm Chemical Reagent Co., Ltd., China. Ammonium thiosulfate ($(NH_4)_2S_2O_3$, 99%) of analytical grade was obtained from Aladdin Co., China. Standard gold solution ($HAuCl_4$, 1000 mg/L) of analytical grade was bought from Well Group Scientific Ltd., USA and used without further purification.

2.2. Preparation of Mn-MoS_2. Mn-MoS_2 spheres were prepared through a one-pot hydrothermal approach. First, $(NH_4)_6Mo_7O_{24}\cdot 4H_2O$ (1 mmol), CN_2H_4S (30 mmol), and a given amount of $MnCl_2\cdot 4H_2O$ were dissolved in deionized water (32 mL) and magnetically stirred for 60 min. Second, the solution was transferred into a Teflon-lined autoclave (50 mL) and maintained at 220 °C for 24 h in an oven. After this, the obtained products were naturally cooled down to room temperature, collected by filtration, and washed with water and ethanol for several times. Finally, the black products were dried at −60 °C in a vacuum. In order to investigate the dosage effect of $MnCl_2\cdot 4H_2O$ on the property of resulting MoS_2, various dosages (0.025, 0.05, 0.075, and 0.1 mmol) of $MnCl_2\cdot 4H_2O$ were added to synthesize Mn-MoS_2 with different doping contents of Mn atoms. On the basis of chemical component analysis via inductively coupled plasma-optical emission spectrometry (ICP-OES), the obtained samples were named $Mo_{0.499}Mn_{0.005}S$, $Mo_{0.491}Mn_{0.008}S$, $Mo_{0.487}Mn_{0.010}S$, and $Mo_{0.480}Mn_{0.013}S$, respectively. Without the addition of $MnCl_2\cdot 4H_2O$, MoS_2 was prepared through the same steps.

2.3. Reduction Experiments. Adding $HAuCl_4$ into $(NH_4)_2S_2O_3$ solution was to prepare $[Au(S_2O_3)_2]^{3-}$ solution as described in previous work;[22] 10 mg of synthesized samples (MoS_2 or Mn-MoS_2) was added into $[Au(S_2O_3)_2]^{3-}$ solution (150 mL) with a Au concentration of 100 mg/L, and subsequently, the solution was stirred (150 rpm) under natural light with an intensity of 0.457 kW/m^2. The composition design of gold solution was based on the recovery ability of the synthesized materials. At various time intervals, the reaction suspension (1−2 mL) was extracted and then filtered with a 0.22 μm filter membrane. An atomic absorption spectrophotometer (AA-6680 Shimadzu, Japan) was applied for detecting the concentration of Au(I).

$[Au(S_2O_3)_2]^{3-}$ reduction was calculated as the following equation:

$$R = \frac{C_0V_0 - CV}{m} \quad (1)$$

where, R is $[Au(S_2O_3)_2]^{3-}$ reduction in the sample, mg/g; C_0 and C denotes Au(I) concentration before and after the reaction, respectively, mg/L; V_0 and V represents the volume of solution before and after reaction, respectively, L; and m is the mass of the sample, g.

2.4. DFT Calculations. The detailed mechanism of enhanced $[Au(S_2O_3)_2]^{3-}$ recovery by Mn-MoS_2 was handled using DFT calculation by the DMol3 package. Mn-MoS_2 was constructed by substituting Mo atoms with Mn atoms, and the models of MoS_2 and Mn-MoS_2 were built as shown in Figure 1a,b. A vacuum layer was set as 20 Å in a slab model to avoid the interaction between neighboring surfaces. A 5 × 5 × 1 supercell was adopted to assess the electronic and adsorption property. The Perdew-Bruke-Ernzerhof (PBE) functional was applied within the generalized gradient approximation (GGA) to account for the exchange. The maximum force is within 0.10 eV/Å, and the K-point mesh calculation for samples in the Brillouin zone was 5 × 5 × 1. The energy convergence accuracy was 1 × 10^{-5} Hartree. Before studying the performance of Au(I) on the surface of Mn-MoS_2, the structural stability was characterized. The stability of Mn-MoS_2 was estimated through calculating the formation energies (E_{form}) as follows:

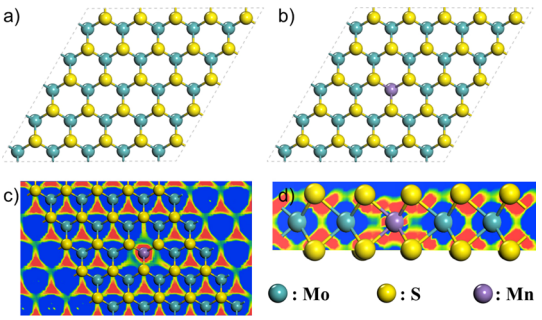

Figure 1. Top views of the supercell models of MoS_2 (a) and Mn-MoS_2 (b); electron density maps of Mn-MoS_2: top (c) and front (d) views after structure optimization.

$$E_{form} = E_{doped} - E_{pure} + \mu_{Mo} - \mu_{Mn} \quad (2)$$

where E_{doped} and E_{pure} were the total energy of Mn-MoS_2 and MoS_2, respectively; μ_{Mo} and μ_{Mn} exhibited the chemical potentials of Mo and Mn, respectively. According to the definition, the formation energy of Mn-MoS_2 was −2.11133 eV, indicating the stability of the Mn-MoS_2 structure. Figure 1c,d displays the electron density maps of Mn-MoS_2 after structure optimization, which demonstrated that Mn atoms could well bond with S atoms.

2.5. Characterization. The structure of samples was identified by XRD with Cu Kα (Bruker AXS, Germany). An XPS spectrometer (Thermo ESCALB 250 Xi, USA) and an inductively coupled plasma-optical emission spectrometer (Agilent 720ES, USA) were used to study the chemical states and element component. The microstructure was imaged on a scanning electron microscope (Phenom ProX G6, The Netherlands) and a transmission electron microscope (JEM-2100F, Japan). Elemental mappings were obtained by energy dispersive spectroscopy (EDS) attached with TEM. UV−vis spectra were recorded on a spectrophotometer (Lambda 750S UV−Vis, USA). Zeta potential was measured by Malvern Zetasizer Nano ZS90

https://doi.org/10.1021/acssuschemeng.1c02160
ACS Sustainable Chem. Eng. XXXX, XXX, XXX−XXX

(UK). An atomic adsorption spectrophotometer (contrAA-700, Germany) was utilized to analyze the concentration of Au(I).

2.6. Electrochemical Measurements. The electrochemical measurements were performed in a three-electron system through an electrochemical station (CHI1030B). The Pt flake, saturated calomel electrode, and ITO glass deposited with samples were used as the counter electrode, reference electrode, and working electrode, respectively. Photocurrent measurements were detected under a xenon lamp with a light intensity of 300 W. The interval of light on/off was set to 30 s. Electrochemical impedance spectroscopy (EIS) was carried out at an alternating current voltage of 10 mN over a frequency range of $0.01-10^5$ Hz in a 1 M potassium ferricyanide solution. Mott−Schottky analysis was measured at a frequency of 1000 Hz.

3. RESULTS AND DISCUSSION

3.1. Structure and Composition Analysis. XRD patterns of the prepared MoS_2 and Mn-MoS_2 spheres are shown in Figure 2. Only the diffraction peaks corresponding to

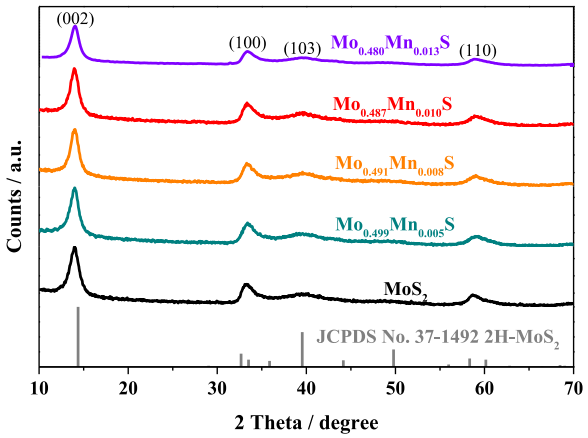

Figure 2. XRD patterns of MoS_2 and Mn-MoS_2.

the 2H phase structure were observed in MoS_2 (2H-MoS_2, JCPDS 37-1492).[30] It is noteworthy that the prepared Mn-MoS_2 revealed the similar peaks to MoS_2, indicating that the incorporation of Mn hardly affected the structure of MoS_2.[31]

The morphology and microstructure of Mn-MoS_2 were characterized by SEM and TEM, and the results are depicted in Figure 3. The SEM results (Figure 3a−e) showed that MoS_2 and Mn-MoS_2 possessed a similar flowerlike sphere morphology, implying that doping Mn atoms would not affect the morphology. Elemental Mo, Mn, and S are shown in Figure 3f, which indicated that the existence of Mn atoms in Mn-MoS_2. As seen from Figure 3g, the Mn-MoS_2 exhibited sheet has a lateral size of nearly 100−200 nm. The high-resolution TEM (HRTEM) images (Figure 3h) revealed that the interlayer spacing value of Mn-MoS_2 was almost 6.9 Å that is assigned to the (002) crystal facet of MoS_2.[32] Moreover, crystal defects could be directly observed as marked by the white circles, which agreed with the existence of rich defects as well as previous report.[33] Other crystal facet corresponding to MoS_2 could be found in the selected area electron diffraction (SAED) pattern (Figure 3i). Mo, S, and Mn elements were clearly seen along the Mn-MoS_2 outline from the corresponding EDS elemental mapping (Figure 3j−n), implying the existence of Mn atoms. The above results demonstrated that the incorporation of Mn had little effect on the structure and morphology of MoS_2.

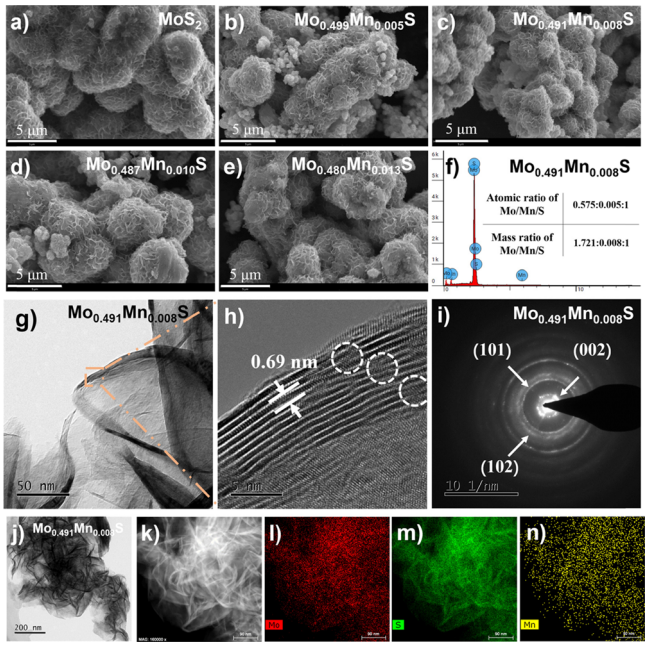

Figure 3. SEM images of MoS_2 and Mn-MoS_2 (a−e), EDS pattern (f), TEM (g), HRTEM (h), SAED (i) images, and corresponding EDS elemental mapping (j−n) of $Mo_{0.491}Mn_{0.008}S$.

Chemical states of elements in MoS_2 and Mn-MoS_2 was further investigated by XPS. The XPS survey spectra of MoS_2 and Mn-MoS_2 (Figure 4a) exhibited the presence of Mo and S, but the peak of Mn was hardly found due to the small dosage. As seen in Figure 4b,c, Mn-MoS_2 exhibited identical peaks in Mo 3d, S 2s, and S 2p regions in accordance with those of MoS_2. Three characteristic peaks were observed at around 226, 229, and 232 eV in Mo 3d and S 2s regions, which could be ascribed to binding energies of S 2s, Mo^{IV} $3d_{5/2}$, and Mo^{IV} $3d_{3/2}$ components in the 2H-MoS_2 phase, respectively.[34] In Figure 4c, S 2p region showed doublet peaks at about 162 and 163 eV, corresponding to the typical binding energy of S $2p_{1/2}$ and S $2p_{3/2}$, respectively.[35] Moreover, the peak at about 642 eV in the Mn 2p spectrum of Mn-MoS_2 was attributed to the incorporation of Mn atoms into MoS_2 (Figure 4d), which was in line with the literature.[36]

3.2. Reduction Performance. The photocatalytic reduction performance was explored under sunlight, and the results are displayed in Figure 5a. The reduction capacity quickly grew as time elapsed and then reached a balance at about 900 min. It was clear that MoS_2 with a small Mn doping amount could accelerate the reduction rate and enhance the reduction capacity. For instance, $Mo_{0.491}Mn_{0.008}S$ exhibited an exceptional reduction capacity with 936.9 mg/g, which was 1.5 times higher than that of MoS_2. The reduction rate of Mn-MoS_2 (2.74 mg/(g min)) increased to 272% compared to that of MoS_2 (1.01 mg/(g min)) in 300 min. The reduction capacity of $[Au(S_2O_3)_2]^{3-}$ increased slowly with the increase of Mn content in Mn-MoS_2 followed by a decline, which might be attributed to the quick combination of photoelectrons originated from the narrow band gap. As shown in Figure 5b, as the initial $[Au(S_2O_3)_2]^{3-}$ concentration increased, the reduction capacity of $[Au(S_2O_3)_2]^{3-}$ increased, which suggested that Mn-MoS_2 could be used for recycling large quantities of Au(I) from thiosulfate leaching solutions. pH ranging from 8 to 12 was applied to investigate the influence of

https://doi.org/10.1021/acssuschemeng.1c02160
ACS Sustainable Chem. Eng. XXXX, XXX, XXX−XXX

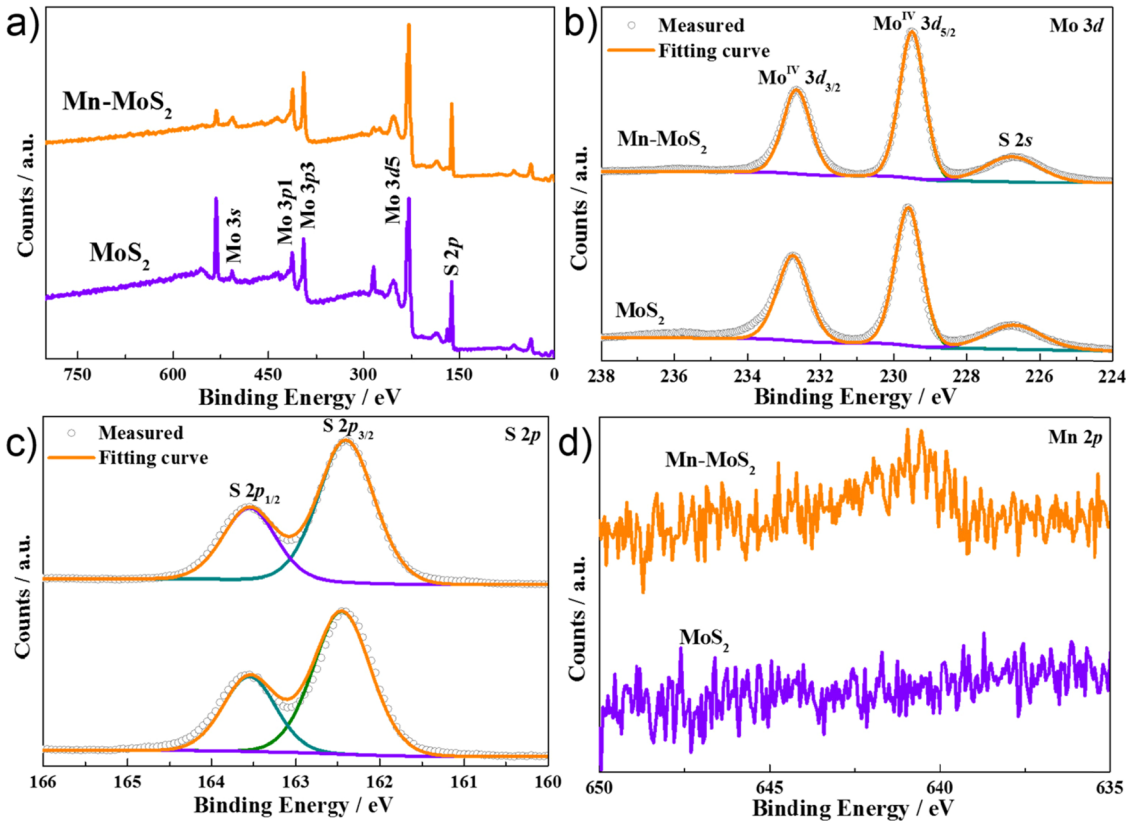

Figure 4. XPS of MoS_2 and Mn-MoS_2: survey spectra (a), Mo 3d spectra (b), S 2p spectra (c), and Mn 2p spectra (d).

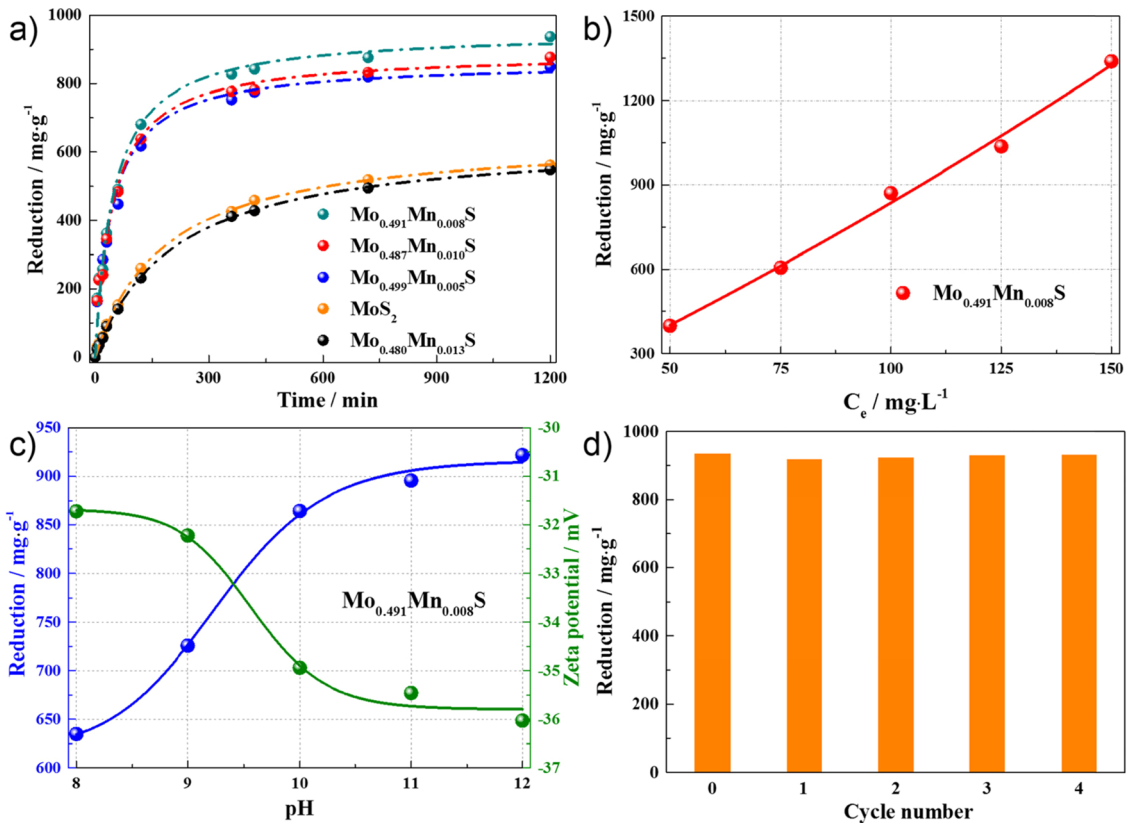

Figure 5. Photocatalytic reduction performance of $[Au(S_2O_3)_2]^{3-}$ on MoS_2 and Mn-MoS_2 as a function of time (a), effect of initial $[Au(S_2O_3)_2]^{3-}$concentration on $Mo_{0.491}Mn_{0.008}S$ (b), effect of pH on reduction of $[Au(S_2O_3)_2]^{3-}$ and zeta potential of $Mo_{0.491}Mn_{0.008}S$ (c), and the cycling test of $Mo_{0.491}Mn_{0.008}S$ (d).

https://doi.org/10.1021/acssuschemeng.1c02160
ACS Sustainable Chem. Eng. XXXX, XXX, XXX−XXX

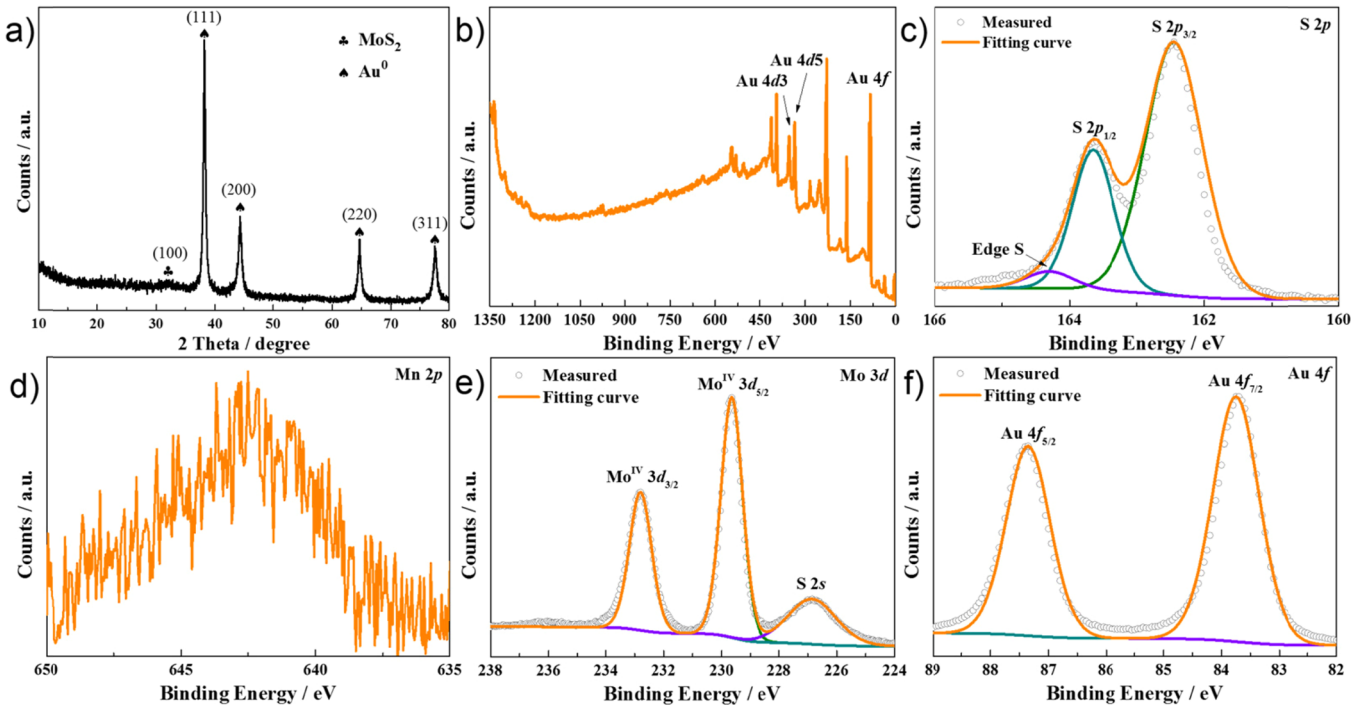

Figure 6. XRD patterns (a), survey spectrum (b), S 2p spectrum (c), Mn 2p spectrum (d), Mo 3d spectrum (e), and Au 4f spectrum (f) of Mn-MoS_2 after reduction of $[Au(S_2O_3)_2]^{3-}$.

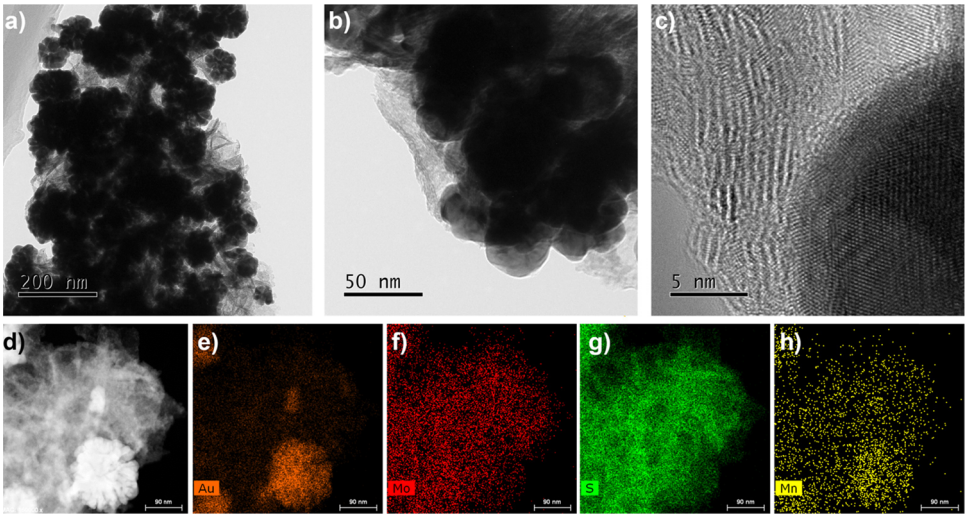

Figure 7. TEM images of Mn-MoS_2 after $[Au(S_2O_3)_2]^{3-}$ reduction (a–c) and corresponding EDS elemental mapping (d–h).

pH on the performance of photocatalytic reduction of $[Au(S_2O_3)_2]^{3-}$, as depicted in Figure 5c. The reduction capacity boosted when pH increased and then tended to balance. The potential of Mn-MoS_2 in aqueous solutions was detected for investigating the phenomenon (Figure 5c). From the perspective of catalysis using MoS_2, the catalytic activity not only originated from Mo edges but also from unsaturated S atoms, so unsaturated S atoms easily interacted with $[Au(S_2O_3)_2]^{3-}$ as well.[5,12] Furthermore, these active sites are negatively charged, which would bond with H^+ in aqueous solutions. When the pH increased, the negative potential of Mn-MoS_2 increased rapidly and then slowed down, explaining the decreased interaction of H^+ with unsaturated S atoms. As a result, more active sites of Mn-MoS_2 interacted with $[Au(S_2O_3)_2]^{3-}$ as the pH increased. The cycling stability of Mn-MoS_2 for reduction of $[Au(S_2O_3)_2]^{3-}$ was evaluated under identical conditions (Figure 5d). The reduction capacity after four cycles was still as high as 933.8 mg/g, exhibiting the excellent stability of Mn-MoS_2.

After $[Au(S_2O_3)_2]^{3-}$ recovery, XRD, XPS, and TEM were used for exploring the component and morphology of $Mo_{0.491}Mn_{0.008}S$. Figure 6a displays the XRD pattern of Mn-MoS_2 after recycling $[Au(S_2O_3)_2]^{3-}$. Four new peaks observed at around 38.2, 44.4, 64.7, and 77.6° were attributed to gold particles (JCPDS 04-0784),[37] confirming the reduction of $[Au(S_2O_3)_2]^{3-}$ into Au^0. The XPS survey spectrum of $Mo_{0.491}Mn_{0.008}S$ after the recycle of $[Au(S_2O_3)_2]^{3-}$ is given in Figure 6b, and the characteristic peaks of Au^0 was detected. Peaks in the spectrum of Mo 3d, S 2p, and Mn 2p as shown in Figure 6c–e were unchanged. The Au binding energies of 83.7

https://doi.org/10.1021/acssuschemeng.1c02160
ACS Sustainable Chem. Eng. XXXX, XXX, XXX−XXX

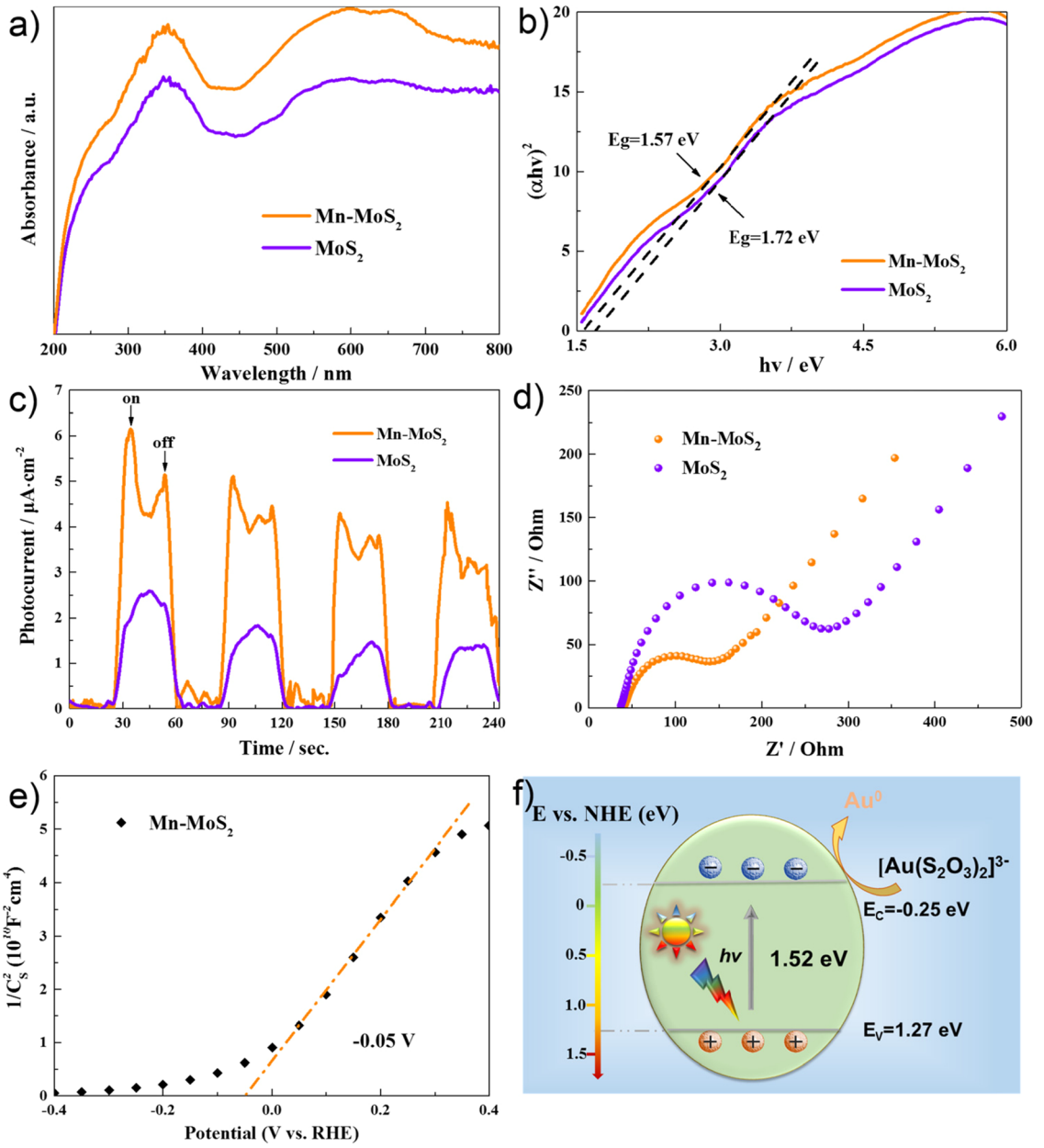

Figure 8. UV−vis absorption spectrum (a), Kubelka-Munk transformed reflectance spectrum (b), photocurrent responses (c) and EIS curves (d) of MoS_2 and Mn-MoS_2, Mott−Schottky plot of Mn-MoS_2 (e), and schematic illustration of the band structure and relevant redox potential of Mn-MoS_2 (f).

and 87.4 eV (Figure 6f) were indexed to Au $4f_{5/2}$ and Au $4f_{7/2}$ of Au^0[38] exhibiting that $[Au(S_2O_3)_2]^{3-}$ was reduced into Au^0 and recycled.

TEM was used for observing the morphology of Mn-MoS_2 after the recovery of $[Au(S_2O_3)_2]^{3-}$. As exhibited in Figure 7a−c, gold nanoparticles with a size of about 50−100 nm were in close contact with the surface of Mn-MoS_2. The elemental mapping in the corresponding EDS (Figure 7d−h) revealed the same distribution area of Mo, S, and Mn, and Au was evenly distributed on the nanoparticle. Therefore, it was further demonstrated that $[Au(S_2O_3)_2]^{3-}$ was recycled as Au^0 using Mn-MoS_2.

3.3. Reduction Mechanism. UV−vis absorption of MoS_2 and $Mo_{0.491}Mn_{0.008}S$ were tested and the optical properties were investigated, as illustrated in Figure 8a. It was obvious that $Mo_{0.491}Mn_{0.008}S$ expressed stronger absorption than MoS_2 in both ultraviolet and visible light regions. Through the following formula,[39] the band gap value of MoS_2 and $Mo_{0.491}Mn_{0.008}S$ were calculated:

$$(\alpha h\nu)^n = A(h\nu - E_g) \quad (3)$$

where α, h, ν, A, and E_g indicated the absorption coefficient, Planck's constant, light frequency, a constant, and band gap, respectively; the index $n = 2$ was used in this work. The results of band gap energies were estimated and are shown in Figure 8b. Compared with the band gap energy of MoS_2 (1.72 eV), $Mo_{0.491}Mn_{0.008}S$ possessed a narrower band gap energy (1.52 eV), which expressed the quicker transfer of photogenerated electrons in $Mo_{0.491}Mn_{0.008}S$.

Additionally, the photoelectrochemical properties of MoS_2 and Mn-MoS_2 were studied by photocurrent response (Figure 8c) and EIS (Figure 8d). Mn-MoS_2 showed greater photo-

https://doi.org/10.1021/acssuschemeng.1c02160
ACS Sustainable Chem. Eng. XXXX, XXX, XXX−XXX

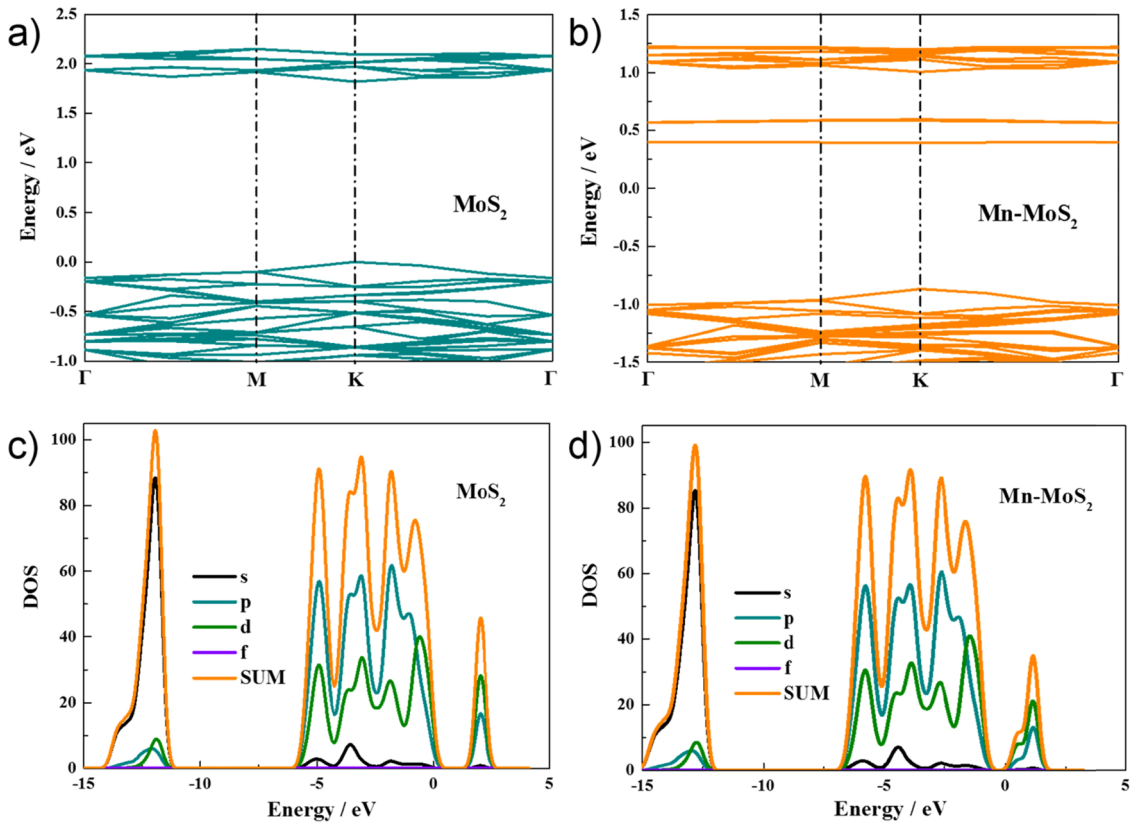

Figure 9. Band structures of MoS_2 (a) and Mn-MoS_2 (b), and TDOS and PDOS curves of MoS_2 (c) and Mn-MoS_2 (d).

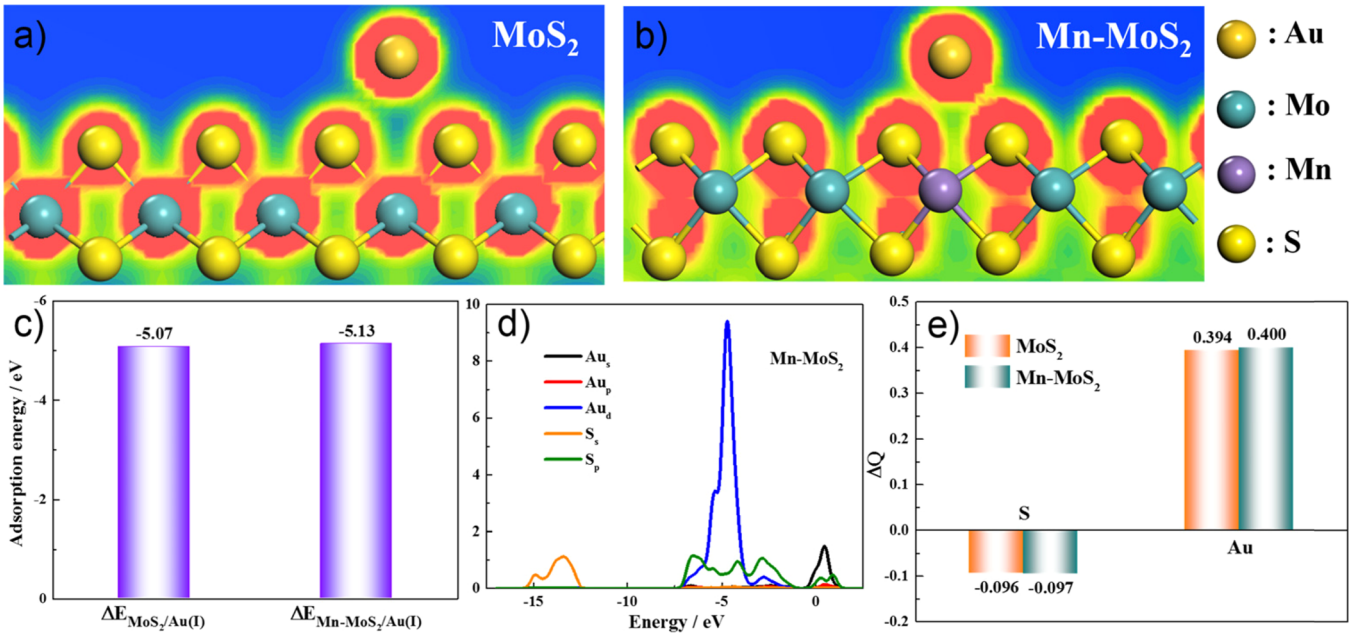

Figure 10. Electron density maps of Au(I) on MoS_2 (a) and Mn-MoS_2 (b): front views. Adsorption energy of Au(I) on MoS_2 and Mn-MoS_2 (c), PDOS between Au(I) and S for Au(I) adsorption in Mn-MoS_2 (d), and Mulliken atomic charge changes of Au(I) and S in the system of Au(I) adsorption on MoS_2 and Mn-MoS_2 (e).

current intensity than MoS_2, resulting from the higher electronic conductivity. The semicircle of Mn-MoS_2 was smaller than that of MoS_2 in EIS results, which implied that the incorporation of Mn atoms could reduce the charge-transfer resistance. It was concluded that efficient reduction of $[Au(S_2O_3)_2]^{3-}$ by Mn-MoS_2 was attributed to excellent transfer of photoelectrons and small transfer resistance of photoelectrons. Figure 8e displays the Mott−Schottky plot of Mn-MoS_2, and the flat band potential (E_{fb}) was found to be at −0.05 V. The positive slope of the curve demonstrated the n-type characteristic of Mn-MoS_2. E_{fb} was close to the CB value in the n-type semiconductor; thus, the CB of Mn-MoS_2 was

https://doi.org/10.1021/acssuschemeng.1c02160
ACS Sustainable Chem. Eng. XXXX, XXX, XXX−XXX

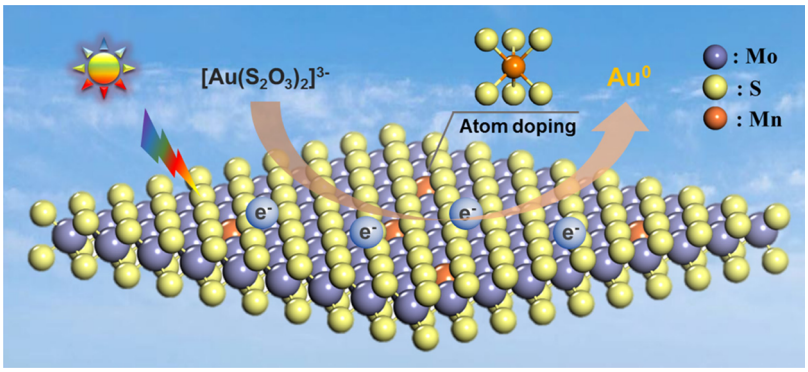

Figure 11. Reduction mechanism of $[Au(S_2O_3)_2]^{3-}$ on Mn-MoS_2.

−0.25 eV. The valance band (VB) edge was calculated by following equation:

$$E_V = E_g + E_C \quad (4)$$

Based on the above equation, the E_V value of Mn-MoS_2 was 1.27 eV. The schematic illustration of the band structure and relevant redox potential of Mn-MoS_2 is exhibited in Figure 8f. According to the electrochemistry basic principle, the CB edge of Mn-MoS_2 was more negative than the reduction potential of $[Au(S_2O_3)_2]^{3-}/Au^0$ (0.15 eV), which demonstrated that $[Au(S_2O_3)_2]^{3-}$ could be photocatalytically reduced into Au^0 on Mn-MoS_2.

To further clarify the effect of the Mn dopant on the enhanced recovery of $[Au(S_2O_3)_2]^{3-}$, DFT calculations were carried out for studying the electronic properties of Mn-MoS_2 and the interaction between Au(I) and Mn-MoS_2. Figure 9a,b shows the results of the band structure of MoS_2 and Mn-MoS_2. The direct band gap at the K-point of MoS_2 was estimated to be E_g = 1.82 eV and it was well consistent with previous research studies.[27] As for Mn-MoS_2, the direct band gap decreased, which agreed with the results of the Kubelka-Munk transformed reflectance, reflecting the faster transfer of photoelectrons. The CB edge value (−0.87 eV) was lower in energies than the reduction potential of $[Au(S_2O_3)_2]^{3-}$ to Au^0 (0.15 eV), proving the reduction of $[Au(S_2O_3)_2]^{3-}$ into Au^0 on Mn-MoS_2. When the Mn atom was incorporated into MoS_2, the band gap was reduced as a result of the introduction of flat impurity bands below the VB edge. For gaining more insight into the electronic properties of MoS_2 and Mn-MoS_2, the total density of states (TDOS) and partial total density of states (PDOS) were calculated and are shown in Figure 9c,d. It was clear that the doping of Mn atoms brought the impurity band near below the VB minimum, which was consistent with ref 40.

The interaction between Au(I) and catalysis (MoS_2 or Mn-MoS_2) was considered as one important factor for improving the photocatalytic reduction of $[Au(S_2O_3)_2]^{3-}$. Figure 10a,b shows the electron density maps of the interaction of Au(I) with MoS_2 and Mn-MoS_2. Obviously, Au(I) mainly interacted with S atoms on MoS_2 and Mn-MoS_2. When Mn atoms were incorporated into the structure of MoS_2, Au(I) tended to bond with S atoms that connected with Mn atoms, which suggested that S atoms near Mn atoms acted as reactive sites. A denser overlap of the electron cloud was found in the interaction between Au(I) and Mn-MoS_2 than between Au(I) and MoS_2, indicating the stronger affinity of Au(I) and Mn-MoS_2. For further illustrating the interaction phenomenon, the adsorption energies between Au(I) and MoS_2 (or Mn-MoS_2) were studied, as shown in Figure 10c. The interaction between Au(I) and Mn-MoS_2 was stronger than that between Au(I) and MoS_2, indicating that the incorporation of the Mn atom benefited the adsorption of Au(I). The result was in good agreement with that obtained from electron density maps. Also, PDOS was calculated to clarify the interacting orbitals of Au(I) and S atoms on Mn-MoS_2, plotted as shown in Figure 10d. Au s and d orbitals bond with the S p orbital near the Fermi level, and this revealed strong interaction of Au and S atoms. In order to study charge changes between Au(I) and MoS_2 (or Mn-MoS_2), Mulliken atomic charge changes (ΔQ) of Au(I) and nearby S atoms were calculated before and after interaction, as displayed in Figure 10e. After interaction, Au(I) was positively charged, and most of the lost charges were transferred to nearby S atoms, demonstrating the interaction between Au(I) and S atoms of MoS_2 and Mn-MoS_2. Positive charge of Au(I) atoms in Mn-MoS_2 was more than that in MoS_2, further verifying the stronger interaction between Au(I) and Mn-MoS_2.

Based on the above discussion, the mechanism for efficiently reducing and recycling $[Au(S_2O_3)_2]^{3-}$ using Mn-MoS_2 is schematically shown in Figure 11. The enhanced photocatalytic reduction ability of $[Au(S_2O_3)_2]^{3-}$ was originated from the enhancement of photoelectrochemical properties and the interaction between Au(I) and Mn-MoS_2. Incorporating Mn atoms in MoS_2 could reduce charge-transfer resistance, enhancing light absorption, and transfer of photo electrons. Au(I) strongly bonds with S atoms near incorporated Mn atoms. The process was concluded as follows. $[Au(S_2O_3)_2]^{3-}$ was absorbed on the surface of Mn-MoS_2; then, photogenerated electrons produced at the VB position were transferred to the CB position upon visible light irradiation. $S_2O_3^{2-}$ might be the sacrificial agent for consuming the photogenerated holes. The photogenerated electrons would combine with $[Au(S_2O_3)_2]^{3-}$, resulting in the reduction of $[Au(S_2O_3)_2]^{3-}$ into Au^0. The possible chemical reaction is given as follows:

$$Mn - MoS_2 \xrightarrow{h\nu} e^- + h^+ \quad (5)$$

$$2S_2O_3^{2-} + 2h^+ \rightarrow S_4O_6^{2-} \quad (6)$$

$$Au^+ + e^- \rightarrow Au^0 \quad (7)$$

4. CONCLUSIONS

In conclusion, Mn-incorporated MoS_2 was facilely fabricated by a hydrothermal route, enhancing the photocatalytic reduction ability of $[Au(S_2O_3)_2]^{3-}$ with a remarkable reduction

https://doi.org/10.1021/acssuschemeng.1c02160
ACS Sustainable Chem. Eng. XXXX, XXX, XXX−XXX

rate and capacity (936.9 mg/g). The improvement originated from the enhanced photoelectrochemical properties including stronger light absorption, more efficient transfer of photogenerated electrons, and lower charge-transfer resistance. Furthermore, it was found that incorporated Mn atoms slightly promoted the interaction between S atoms and Au(I). This study might benefit the development for efficient recycling of gold from thiosulfate leaching solutions.

AUTHOR INFORMATION

Corresponding Author

Feifei Jia − *Hubei Key Laboratory of Mineral Resources Processing and Environment, Wuhan University of Technology, Wuhan, Hubei 430070, China;* orcid.org/0000-0003-0427-8117; Email: feifeijia@whut.edu.cn

Authors

Weiquan Zhan − *Hubei Key Laboratory of Mineral Resources Processing and Environment, Wuhan University of Technology, Wuhan, Hubei 430070, China; Instituto de Fisica, Universidad Autonoma de San Luis Potosi, C.P. 78290 San Luis Potosi, S.L.P., Mexico*

Yuan Yuan − *Hubei Key Laboratory of Mineral Resources Processing and Environment, Wuhan University of Technology, Wuhan, Hubei 430070, China; Instituto de Fisica, Universidad Autonoma de San Luis Potosi, C.P. 78290 San Luis Potosi, S.L.P., Mexico*

Xin Yao − *High Technology Research and Development Center, Beijing 100044, China*

Bingqiao Yang − *School of Xingfa Mining Engineering, Wuhan Institute of Technology, Wuhan, Hubei 430073, China*

Changsheng Lin − *Hubei Key Laboratory of Mineral Resources Processing and Environment, Wuhan University of Technology, Wuhan, Hubei 430070, China*

José Luis Arauz-Lara − *Instituto de Fisica, Universidad Autonoma de San Luis Potosi, C.P. 78290 San Luis Potosi, S.L.P., Mexico*

Shaoxian Song − *Hubei Key Laboratory of Mineral Resources Processing and Environment, Wuhan University of Technology, Wuhan, Hubei 430070, China;* orcid.org/0000-0001-7278-7875

Complete contact information is available at: https://pubs.acs.org/10.1021/acssuschemeng.1c02160

Notes

The authors declare no competing financial interest.

ACKNOWLEDGMENTS

The financial supports to this work from the National Natural Science Foundation of China (Nos. 51974216, 51704212, and 51704220), the Natural Science Foundation of Hubei Province (No. 2019CFB536), and the Fundamental Research Funds for the Central Universities (111-212408003 and 2021III033JC) are gratefully acknowledged.

REFERENCES

(1) Do, S. H.; Jo, Y. H.; Park, H. D.; Kong, S. H. Synthesis of Iron Composites on Nano-Pore Substrates: Identification and Its Application to Removal of Cyanide. *Chemosphere* **2012**, *89*, 1450−1456.

(2) Wang, C.; Lin, G.; Zhao, J.; Wang, S.; Zhang, L.; Xi, Y.; Li, X.; Ying, Y. Highly Selective Recovery of Au(III) from Wastewater by Thioctic Acid Modified Zr-MOF: Experiment and DFT Calculation. *Chem. Eng. J.* **2020**, *380*, No. 122511.

(3) Schuppe, A. W.; Borrajo-Calleja, G. M.; Buchwald, S. L. Enantioselective Olefin Hydrocyanation without Cyanide. *J. Am. Chem. Soc.* **2019**, *141*, 18668−18672.

(4) Fuertes, A. B.; Ferrero, G. A.; Diez, N.; Sevilla, M. A Green Route to High-Surface Area Carbons by Chemical Activation of Biomass-Based Products with Sodium Thiosulfate. *ACS Sustainable Chem. Eng.* **2018**, *6*, 16323−16331.

(5) Chen, S.; Zi, F.; Hu, X.; Chen, Y.; Yang, P.; Wang, Q.; Qin, X.; Cheng, H.; Liu, Y.; He, Y.; et al. Interfacial Properties of Mercaptopropyl-Functionalised Silica Gel and Its Adsorption Performance in the Recovery of gold(I) Thiosulfate Complex. *Chem. Eng. J.* **2020**, *393*, No. 124547.

(6) Karavasteva, M. Kinetics and Deposit Morphology of Gold Cemented on Magnesium, Aluminum, Zinc, Iron and Copper from Ammonium Thiosulfate-Ammonia Solutions. *Hydrometallurgy* **2010**, *104*, 119−122.

(7) Guerra, E.; Dreisinger, D. B. A Study of the Factors Affecting Copper Cementation of Gold from Ammoniacal Thiosulphate Solution. *Hydrometallurgy* **1999**, *51*, 155−172.

(8) Xu, B.; Li, K.; Li, Q.; Yang, Y.; Liu, X.; Jiang, T. Kinetic Studies of Gold Leaching from a Gold Concentrate Calcine by Thiosulfate with Cobalt-Ammonia Catalysis and Gold Recovery by Resin Adsorption from Its Pregnant Solution. *Sep. Purif. Technol.* **2019**, *213*, 368−377.

(9) Zhao, M.; Zhao, J.; Huang, Z.; Wang, S.; Zhang, L. One Pot Preparation of Magnetic Chitosan-Cystamine Composites for Selective Recovery of Au(III) from the Aqueous Solution. *Int. J. Biol. Macromol.* **2019**, *137*, 721−731.

(10) AL-Othman, Z. A.; Ali, R.; Naushad, M. Hexavalent Chromium Removal from Aqueous Medium by Activated Carbon Prepared from Peanut Shell: Adsorption Kinetics, Equilibrium and Thermodynamic Studies. *Chem. Eng. J.* **2012**, *184*, 238−247.

(11) Ramírez-Muñiz, K.; Song, S.; Berber-Mendoza, S.; Tong, S. Adsorption of the Complex Ion $Au(CN)_2^-$ onto Sulfur-Impregnated Activated Carbon in Aqueous Solutions. *J. Colloid Interface Sci.* **2010**, *349*, 602−606.

(12) Fotoohi, B.; Mercier, L. Some Insights into the Chemistry of Gold Adsorption by Thiol and Amine Functionalized Mesoporous Silica in Simulated Thiosulfate System. *Hydrometallurgy* **2015**, *156*, 28−39.

(13) Sun, D. T.; Gasilova, N.; Yang, S.; Oveisi, E.; Queen, W. L. Rapid, Selective Extraction of Trace Amounts of Gold from Complex Water Mixtures with a Metal-Organic Framework (MOF)/Polymer Composite. *J. Am. Chem. Soc.* **2018**, *140*, 16697−16703.

(14) Zhan, W.; Yuan, Y.; Yang, B.; Jia, F.; Song, S. Construction of MoS_2 Nano-Heterojunction via ZnS Doping for Enhancing in-Situ Photocatalytic Reduction of Gold Thiosulfate Complex. *Chem. Eng. J.* **2020**, *394*, No. 124866.

(15) Chen, P.; Liang, Y.; Yang, B.; Jia, F.; Song, S. In-situ Reduction of Au(I) for Efficient Recovery of Gold from Thiosulfate Solution by the 3D MoS_2/Chitosan Aerogel. *ACS Sustainable Chem. Eng.* **2020**, *8*, 3673−3680.

(16) Zhang, J.; Wang, T.; Liu, P.; Liu, S.; Dong, R.; Zhuang, X.; Chen, M.; Feng, X. Engineering Water Dissociation Sites in MoS_2 Nanosheets for Accelerated Electrocatalytic Hydrogen Production. *Energy Environ. Sci.* **2016**, *9*, 2789−2793.

(17) Yuan, Y.; Yang, B.; Jia, F.; Song, S. Reduction Mechanism of Au Metal Ions into Au Nanoparticles on Molybdenum Disulfide. *Nanoscale* **2019**, *11*, 9488−9497.

(18) Muir, D. M.; Aylmore, M. G. Thiosulphate as an Alternative to Cyanide for Gold Processing − Issues and Impediments. *Miner. Process. Extr. Metall.* **2004**, *113*, 2−12.

(19) Inkpen, M. S.; Liu, Z.−F.; Li, H.; Campos, L. M.; Neaton, J. B.; Venkataraman, L. Non-Chemisorbed Gold−sulfur Binding Prevails in Self-Assembled Monolayers. *Nat. Chem.* **2019**, *11*, 351−358.

(20) Zeng, S.; Jia, F.; Yang, B.; Song, S. In-Situ Reduction of Gold Thiosulfate Complex on Molybdenum Disulfide Nanosheets for a

https://doi.org/10.1021/acssuschemeng.1c02160
ACS Sustainable Chem. Eng. XXXX, XXX, XXX−XXX

Highly-Efficient Recovery of Gold from Thiosulfate Solutions. *Hydrometallurgy* **2020**, *195*, No. 105369.
(21) Chen, P.; Liang, Y.; Yang, B.; Jia, F.; Song, S. In-Situ Photo-Reduction of Au(I) for Efficient Recovery of Gold Thiosulfate by 3D MoS_2/Chitosan Aerogel. *ACS Sustainable Chem. Eng.* **2020**, *8*, 3673−3680.
(22) Sun, K.; Mao, S.; Zhan, W.; Liu, C.; Jia, F.; Song, S. In-Situ Reduction of $Au(S_2O_3)_2^{3-}$ for Efficient Recovery of Gold with Magnetically Separable Shell-Core Structured MoS_2@Fe_3O_4 Composite. *Hydrometallurgy* **2020**, *198*, No. 105514.
(23) Yang, J.; Wang, Y.; Lagos, M. J.; Manichev, V.; Fullon, R.; Song, X.; Voiry, D.; Chakraborty, S.; Zhang, W.; Batson, P. E.; et al. Single Atomic Vacancy Catalysis. *ACS Nano* **2019**, *13*, 9958−9964.
(24) Ji, L.; Yan, P.; Zhu, C.; Ma, C.; Wu, W.; Wei, C.; Shen, Y.; Chu, S.; Wang, J.; Du, Y.; et al. One-Pot Synthesis of Porous 1T-Phase MoS_2 Integrated with Single-Atom Cu Doping for Enhancing Electrocatalytic Hydrogen Evolution Reaction. *Appl. Catal. B Environ.* **2019**, *251*, 87−93.
(25) Xiao, W.; Liu, P.; Zhang, J.; Song, W.; Feng, Y. P.; Gao, D.; Ding, J. Dual-Functional N Dopants in Edges and Basal Plane of MoS_2 Nanosheets Toward Efficient and Durable Hydrogen Evolution. *Adv. Energy Mater.* **2017**, *7*, 1−10.
(26) Sabaraya, I. V.; Shin, H.; Li, X.; Hoq, R.; Incorvia, J. A. C.; Kirisits, M. J.; Saleh, N. B. Role of Electrostatics in the Heterogeneous Interaction of Two-Dimensional Engineered MoS_2 Nanosheets and Natural Clay Colloids: Influence of pH and Natural Organic Matter. *Environ. Sci. Technol.* **2021**, *55*, 919−929.
(27) Liu, M.; Hybertsen, M. S.; Wu, Q. A Physical Model for Understanding the Activation of MoS_2 Basal-Plane Sulfur Atoms for the Hydrogen Evolution Reaction. *Angew. Chem. Int. Ed.* **2020**, *59*, 14835−14841.
(28) Hoa, V. H.; Tran, D. T.; Nguyen, D. C.; Kim, D. H.; Kim, N. H.; Lee, J. H. Molybdenum and Phosphorous Dual Doping in Cobalt Monolayer Interfacial Assembled Cobalt Nanowires for Efficient Overall Water Splitting. *Adv. Funct. Mater.* **2020**, *30*, No. 2002533.
(29) Bolar, S.; Shit, S.; Kumar, J. S.; Murmu, N. C.; Ganesh, R. S.; Inokawa, H.; Kuila, T. Optimization of Active Surface Area of Flower like MoS_2 Using V-Doping towards Enhanced Hydrogen Evolution Reaction in Acidic and Basic Medium. *Appl. Catal. B Environ.* **2019**, *254*, 432−442.
(30) Zhan, W.; Jia, F.; Yuan, Y.; Liu, C.; Sun, K.; Yang, B.; Song, S. Controllable Incorporation of Oxygen in MoS_2 for Efficient Adsorption of Hg^{2+} in Aqueous Solutions. *J. Hazard. Mater.* **2020**, *384*, No. 121382.
(31) Zhou, W. Y.; Li, S. S.; Xiao, X. Y.; Chen, S. H.; Liu, J. H.; Huang, X. J. Defect- and Phase-Engineering of Mn-Mediated MoS_2 Nanosheets for Ultrahigh Electrochemical Sensing of Heavy Metal Ions: Chemical Interaction-Driven in Situ Catalytic Redox Reactions. *Chem. Commun.* **2018**, *54*, 9329−9332.
(32) Jia, F.; Wang, Q.; Wu, J.; Li, Y.; Song, S. Two-Dimensional Molybdenum Disulfide as a Superb Adsorbent for Removing Hg^{2+} from Water. *ACS Sustainable Chem. Eng.* **2017**, *5*, 7410−7419.
(33) Liu, J.; Wang, Z.; Li, J.; Cao, L.; Lu, Z.; Zhu, D. Structure Engineering of MoS_2 via Simultaneous Oxygen and Phosphorus Incorporation for Improved Hydrogen Evolution. *Small* **2020**, *16*, No. 1905738.
(34) Lin, H.; Li, Y.; Li, H.; Wang, X. Multi-Node CdS Hetero-Nanowires Grown with Defect-Rich Oxygen-Doped MoS_2 Ultrathin Nanosheets for Efficient Visible-Light Photocatalytic H_2 Evolution. *Nano Res.* **2017**, *10*, 1377−1392.
(35) Meng, X.; Yu, L.; Ma, C.; Nan, B.; Si, R.; Tu, Y.; Deng, J.; Deng, D.; Bao, X. Three-Dimensionally Hierarchical MoS_2/graphene Architecture for High-Performance Hydrogen Evolution Reaction. *Nano Energy* **2019**, *61*, 611−616.
(36) Sun, T.; Wang, J.; Chi, X.; Lin, Y.; Chen, Z.; Ling, X.; Qiu, C.; Xu, Y.; Song, L.; Chen, W.; Su, C. Engineering the Electronic Structure of MoS_2 Nanorods by N and Mn Dopants for Ultra-Efficient Hydrogen Production. *ACS Catal.* **2018**, *8*, 7585−7592.
(37) Yamazoe, S.; Takano, S.; Kurashige, W.; Yokoyama, T.; Nitta, K.; Negishi, Y.; Tsukuda, T. Hierarchy of Bond Stiffnesses within Icosahedral-Based Gold Clusters Protected by Thiolates. *Nat. Commun.* **2016**, *7*, 10414.
(38) Giner-Casares, J. J.; Henriksen-Lacey, M.; García, I.; Liz-Marzán, L. M. Plasmonic Surfaces for Cell Growth and Retrieval Triggered by near-Infrared Light. *Angew. Chem. Int. Ed.* **2016**, *55*, 974−978.
(39) Zhao, W.; Liu, Y.; Wei, Z.; Yang, S.; He, H.; Sun, C. Fabrication of a Novel P-N Heterojunction Photocatalyst N-$BiVO_4$@p-MoS_2 with Core-Shell Structure and Its Excellent Visible-Light Photocatalytic Reduction and Oxidation Activities. *Appl. Catal. B Environ.* **2016**, *185*, 242−252.
(40) Xie, L.-Y.; Zhang, J.-M. Electronic Structures and Magnetic Properties of the Transition-Metal Atoms (Mn, Fe, Co and Ni) Doped WS_2: A First-Principles Study. *Superlattices Microstruct.* **2016**, *98*, 148−157.

https://doi.org/10.1021/acssuschemeng.1c02160
ACS Sustainable Chem. Eng. XXXX, XXX, XXX−XXX